Non-invasive Hall current distribution measurement in a Hall effect thruster

Carl R. Mullins, Casey C. Farnell, Cody C. Farnell, Rafael A. Martinez, David Liu, Richard D. Branam, and John D. Williams

Citation: Review of Scientific Instruments **88**, 013507 (2017); doi: 10.1063/1.4974098
View online: http://dx.doi.org/10.1063/1.4974098
View Table of Contents: http://aip.scitation.org/toc/rsi/88/1
Published by the American Institute of Physics

Non-invasive Hall current distribution measurement in a Hall effect thruster

Carl R. Mullins,[1] Casey C. Farnell,[2] Cody C. Farnell,[2] Rafael A. Martinez,[1] David Liu,[3] Richard D. Branam,[4] and John D. Williams[1,2]
[1]*Mechanical Engineering, Colorado State University, Fort Collins, Colorado 80523, USA*
[2]*Plasma Controls LLC, 1180 La Eda Lane, Fort Collins, Colorado 80526, USA*
[3]*Air Force Institute of Technology, Wright-Patterson AFB, Ohio 45433, USA*
[4]*University of Alabama, Tuscaloosa, Alabama 35487, USA*

(Received 11 September 2016; accepted 29 December 2016; published online 27 January 2017)

A means is presented to determine the Hall current density distribution in a closed drift thruster by remotely measuring the magnetic field and solving the inverse problem for the current density. The magnetic field was measured by employing an array of eight tunneling magnetoresistive (TMR) sensors capable of milligauss sensitivity when placed in a high background field. The array was positioned just outside the thruster channel on a 1.5 kW Hall thruster equipped with a center-mounted hollow cathode. In the sensor array location, the static magnetic field is approximately 30 G, which is within the linear operating range of the TMR sensors. Furthermore, the induced field at this distance is approximately tens of milligauss, which is within the sensitivity range of the TMR sensors. Because of the nature of the inverse problem, the induced-field measurements do not provide the Hall current density by a simple inversion; however, a Tikhonov regularization of the induced field does provide the current density distributions. These distributions are shown as a function of time in contour plots. The measured ratios between the average Hall current and the average discharge current ranged from 6.1 to 7.3 over a range of operating conditions from 1.3 kW to 2.2 kW. The temporal inverse solution at 1.5 kW exhibited a breathing mode frequency of 24 kHz, which was in agreement with temporal measurements of the discharge current. *Published by AIP Publishing.* [http://dx.doi.org/10.1063/1.4974098]

I. INTRODUCTION

The Hall Effect Thruster (HET) is a plasma device with an annular channel containing orthogonal electric and magnetic fields where electrons ionize an inert gas and the electric field accelerates the created ions. The orthogonal fields force the electrons to circulate azimuthally around the channel and form an embedded plasma current structure known as the Hall current. The electrons introduced to the channel from the cathode make several passes around the channel while colliding with gas atoms and the dielectric walls on their way to the anode. The electron dynamics involved in the Hall current have a large effect on thruster efficiency. Thus imaging the Hall current is a possible way to better understand HETs.

The thrust produced by an HET is generated by the reactive force created by accelerating the ions that is coupled through the thruster magnetic field by the Hall current to the thruster body. The thrust can be estimated using the known magnetic field and the azimuthal Hall current density present in the channel as shown in Eq. (1),

$$T = \int_V |J_H|\, B_r dV, \tag{1}$$

where J_H is the azimuthal current density and B_r is the radial magnetic field. The magnetic field distribution is predetermined during the thruster design and characterization. Therefore, the only unknown is the azimuthal current density distribution. Several invasive[1,2] and non-invasive[3–6] studies have characterized the Hall current distribution. Invasive options utilize fast scanning emissive and Langmuir probes to obtain plasma properties used to calculate electron E × B drift velocities and thereby the current density distribution. These methods perturb the thruster and result in measurement errors.[1,2] In addition, only steady-state estimates of Hall current distributions can be made with this technique. Up to this point, all non-invasive experimental techniques utilized inductive coils surrounding the channel. The coils pick up the transient magnetic fields generated by the azimuthal current when the discharge current is suddenly switched off. This method requires a fast-switching power supply to interrupt the thruster discharge current on a time scale of 100 ns.[3]

Our non-invasive technique measures the induced magnetic field generated by the azimuthal current with an array of sensors and solves the inverse magneto-static problem to obtain the Hall current density distribution. This solution method has been previously developed and simulated using FEMM4.2.[7] Our paper details the development of magnetic sensor experimental hardware and presents results of testing on a 1.5 kW HET.[8]

A. Magnetostatic problem

The direct magnetostatic problem is described by the Biot-Savart law, Eq. (2), which is a simplification of the generalized Ampere's equation. The induced magnetic field, B, due to a known current, I, located at a known position in space yields the three dimensional magnetic field in the

surrounding space,

$$\boldsymbol{B}(\boldsymbol{r}) = \frac{\mu_0}{4\pi}\int_C \frac{I d\boldsymbol{l} x \boldsymbol{r}'}{|\boldsymbol{r}'|^3}. \quad (2)$$

The direct problem is commonly used in finite element software to solve for the magnetic field. MagNet and the open source FEMM software were in fact used to simulate the Colorado State University (CSU) HET in the design phase of the thruster.[8] The magnetostatic solution is justified due to the low amplitude of the displacement current within the thruster channel relative to the Hall current. A worst-case approximation of the displacement current contribution to our results is several orders of magnitude lower than the error bounds of our sensor system.

The inverse magnetostatic problem consists of solving for the current density using the surrounding measured magnetic field as input. This problem has been analyzed numerous times in previous work concerning integrated circuits,[9] biomagnetics,[10,11] ferromagnetic material diagnostics,[12] thin shell ferromagnetic structure,[13] and plasma diagnostics.[7] The inverse magnetostatic problem requires regularization and uses *a priori* knowledge of the solution to apply a continuous smoothing function to the results. Since this problem resembles the Fredholm integral equations of the first kind, Tikhonov's regularization method is used, which was determined to be the best choice by Rubin.[7,14] The general form for this problem can be written as

$$\min\left\{||AJ_H - B_m||^2 + \lambda^2\Omega(J)^2\right\}, \quad (3)$$

where A is the Green's matrix relating the current density distribution to the surrounding magnetic field; J_H is the stacked column vector representing the two-dimensional azimuthal Hall current density distribution $j(r,z)$; B_m is the measured and distributed magnetic field vector; and λ is the regularization parameter that controls the amount of smoothing applied to the solution by the regularization term $\Omega(J)^2$. The regularization term used to solve the Hall current distribution is known as the quadratic variation term and takes the form of

$$\Omega(J) = \left\|\frac{\partial^2 J_H}{\partial r^2}\right\|^2 + \left\|\frac{\partial^2 J_H}{\partial z}\right\|^2 + 2\left\|\frac{\partial^2 J_H}{\partial r \partial z}\right\|^2, \quad (4)$$

which has the effect of smoothing the second derivative of the solution to force a continuous distribution. We assumed that all of the electrons circulate azimuthally around the channel in the same direction; therefore, a non-negativity constraint is applied to the solution. We also assume that the Hall current goes to zero at the channel walls and far upstream and downstream of the maximum centerline magnetic field location, which is forced by an applied zero current density boundary condition.

Determining the appropriate amount of regularization is critical to obtaining an accurate solution. The optimal regularization parameter is determined using the L-curve criterion.[15] A parametric plot of the discrete smoothing norm versus the corresponding residual norm for multiple regularization parameters is generated. With both axes on a logarithmic scale, the curve forms a distinctive L-shape and the bend corresponds to the minimum of the two norms. Visual inspection or programmatic detection of the curve bend then yields the desired regularization parameter.[7]

II. EXPERIMENTAL DESIGN

A. Thruster

The CSU 1.5 kW HET is an Stationary Plasma Thruster (SPT)-style design with a ceramic borosil (BN-SiO_2) channel. The channel dimensions are 104 mm O.D. with a width of 17 mm and a length of 32 mm. Four outer coils coupled with a center coil generate the channel magnetic field, which features a plasma lens topography. A center-mounted, heaterless, electride hollow cathode provides electron emission. The thruster is capable of operating at power levels ranging from 0.5 kW to 2.5 kW with both krypton and xenon. The nominal operating point of ~1.5 kW and 300 V of Kr was used for the majority of testing and experimentation. The thrust and efficiency have been previously characterized by Martinez *et al.*[8]

B. Hall current density sensor

Inside the Hall thruster channel, electrons make several azimuthal passes before collecting on the anode. The design of the magnetic field causes these electrons to flow in a localized region near the maximum magnetic field location of the thruster. The azimuthally drifting electrons form what is known as the Hall current illustrated in Fig. 1. This current generates an induced magnetic field, up to ~2 G in nearby regions external to the channel, that is significantly less than the background field generated by the thruster coils within the channel, ~150 G. Tunneling magnetoresistive (TMR) sensors, made by Micromagnetics, were chosen for our study based on their high sensitivity and their ability to operate in a high magnetic strength background field (Fig. 1). The sensors have a unidirectional sensing area of 1 μm^2. The sensors can operate in a maximum field of 30 G and temperatures up to 150 °C before failure. All the sensors in our fixed array share a single buss powered by a 3.7 V Li-ion battery as shown in Fig. 2, and they are thermally controlled to 25 °C ± 5 °C with an external water chiller.

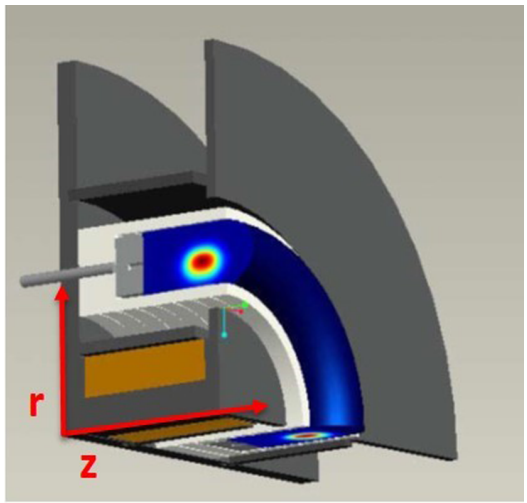

FIG. 1. Quarter-section of Hall thruster illustrates the Hall current density distribution across the acceleration channel.

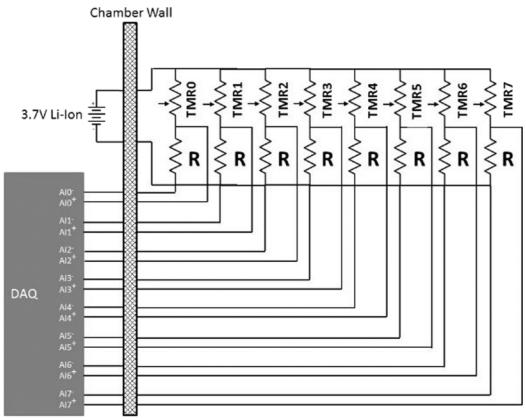

FIG. 2. Eight sensor magnetic circuit schematic. All 8 sensors are wired in parallel in a voltage divider configuration where R = 1.4 kΩ. The battery and DAQ are outside vacuum.

The sensor system utilized all 8 channels available in the National Instrument (NI) USB-6366 data acquisition (DAQ), which were simultaneously sampled at 2 MHz each. Using 8 sensors provided more diverse information about the induced field to allow for improved convergence of the inverse solution. Readers are referred to the work of Rubin[7] for more details on a study suggesting that 8 to 13 well-positioned sensors are best for obtaining Hall current distributions in simulations that included measurement attributes of real sensors. Placement of a magnetic sensor array near the exit plane of the thruster, as shown in Fig. 3, allowed for stationary measurement of the induced field. The harsh environment near the thruster limits sensor placement. Simulations of the magnetic fields, with and without a simulated Hall current, downstream of the front outer pole piece of the thruster were used to find the optimal position of the sensors to maximize the sensed change in magnetic field due to the Hall current without exceeding the maximum allowable background field. In Fig. 3, the sensor placement on the circuit board contained 4 radial field sensors and 4 axial field sensors. The 2D contour maps with the sensor locations are shown in Figs. 4 and 5. The radial sensors were in an equally spaced four quadrant grid close to the downstream face of the outer pole piece as shown in Fig. 5. The majority of the magnetic flux coming

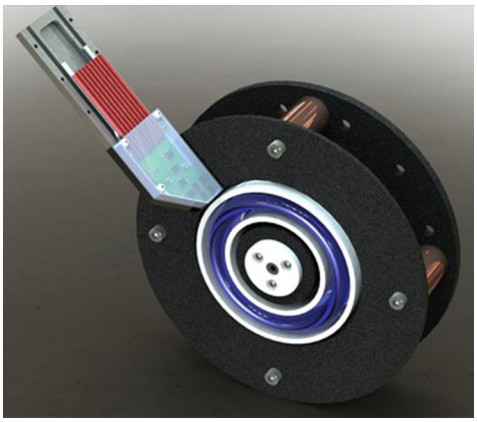

FIG. 3. Magnetic sensor array rendering shows the design and positioning of the sensors relative to the CSU 1.5 kW thruster.

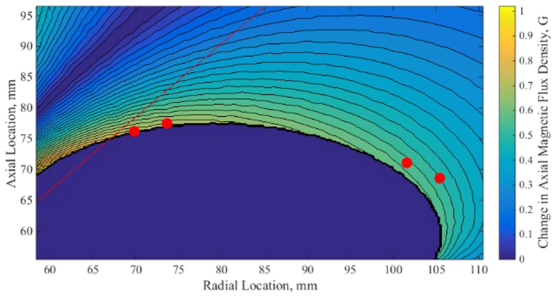

FIG. 4. Simulated induced axial B-field map. Plot of the axially induced magnetic field due to a 35 A Hall current centered in the channel near maximum centerline radial magnetic field. Points display axial sensor locations and red line indicates 40° plume divergence angle.

out of the iron in this location was in the axial direction, allowing the radial sensors to be placed closer to the thruster. Figure 5 illustrates the chosen location of the radial sensors, where the zero axial location was located at the backplate of the thruster. The dark area in the plots corresponds to locations with an absolute magnetic field above the operating range of the TMR sensors, 30 G. The axial sensors were placed along a curve downstream on the printed circuit board running from the inner wall of the board to the outer wall. Figure 4 illustrates the curved placement of the axial sensors stretching from the inner casing wall, left side of the figure, to the casing outer wall, right side of the figure. These locations maximized the sensed induced magnetic field due to the Hall current while keeping the sensors within their operational range. As shown in Fig. 2, each sensor was wired in a voltage divider configuration where the voltage drop was measured across the passive resistor. The passive resistor value chosen created a 1:2 ratio relative to the sensor resistance maximizing the voltage output while keeping the signal within the 2 V full scale range of the DAQ. Triax cabling was used to minimize noise in the power and signal lines. Thermal variance can reduce the sensitivity of the TMRs; therefore, an active cooling system was implemented to maintain the circuit at a constant temperature. The small change due to the induced field, accurately measured by minimizing the signal noise and maximizing the system sensitivity, is of great importance. Making the sensors stationary as opposed to moveable minimized spatial location error, due to the motion stage, and eliminated cycling the sensors through the

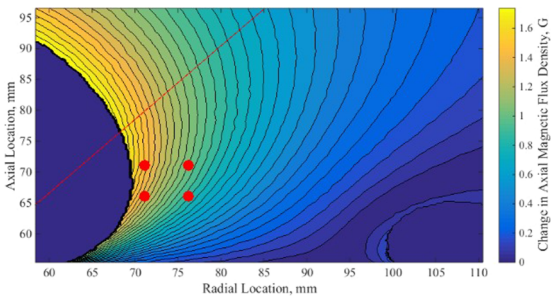

FIG. 5. Simulated induced radial B-field map. Plot of the axially induced magnetic field due to a 35 A Hall current centered in the channel near maximum centerline radial magnetic field. Points display radial sensor locations and red line indicates 40° plume divergence angle.

high external field generated by the thruster, thereby reducing hysteresis error. The simultaneous sampling of all the sensors allowed for a temporal solution of the Hall current distribution.

III. DATA ANALYSIS

A crucial step in operating the sensor involves calibrating the setup to obtain the Green's matrix for the inverse solver. The inverse regularization solution method requires that the Green's matrix, A, be known. This is only achievable with our laboratory thruster by calibration. The Green's matrix is specific to each configuration of the thruster and sensor. The calibration sets the spatial and magnitude relation between the measured magnetic field and the distribution of the current. Therefore, if the sensor location is changed, the thruster magnetic circuit is modified or the surrounding environment is altered; a calibration must be redone. It is possible to achieve a calibration through a simulation,[7] but this was not attempted in our study. Although not attempted, we describe how to construct a Green's matrix using simulations because this is illustrative of how one experimentally accomplishes the same task.

A. Simulated calibration

Simulating the calibration routine is possible and desirable if a high fidelity model of the thruster and the environment can be created, allowing one to calculate the Green's matrix computationally. The difficulty with this process is accounting for all the variables in the system. The B-H curves of the magnetic materials used to construct the thruster can vary from the simulated materials and as a function of temperature. Also, a full three-dimensional magnetostatic model of the thruster can be computationally intensive to obtain.

A simplified magnetostatic model was created to verify the operation of the inverse solution algorithm. The open source magnetostatic software, FEMM, was used to model the 1.5 kW thruster and the calibration procedure in two dimensions. A radial cross section of the thruster, shown in Fig. 6, along with an array of copper wires in the channel is used to simulate point sources of current representative of a discretized Hall current. Ten 22 gauge copper wires are equally spaced in the radial direction on the same axial plane within the thruster channel. The axial and radial magnetic field values are recorded at the intended sensor positions downstream of the front outer pole face in the top right section of Fig. 6. This provided the background field due to the thruster. Next, a known current was applied to each copper wire individually. The magnetic field values were queried at the sensor positions once again. The wires were then moved to a different axial plane and the process was repeated to create a calibration grid within the channel. The Hall current resides near the maximum radial magnetic field and the calibration grid domain was determined based on the predicted location of the Hall current.[1,16] Once the baseline field and the fields associated with each wire in each location were calculated, the change in magnetic field was calculated. The induced magnetic field seen at the sensor locations due to a known current density was now known and the Green's matrix was constructed. Results of the calibration yield a two-dimensional array containing the induced magnetic field for all of the wire coordinate locations. Each sensor has a corresponding 2D calibration matrix organized into a column vector. All of the vectors are then stacked row wise to form the Green's matrix. The number of rows corresponds to the number of sensors used, eight for the stationary array, and the number of columns is equivalent to the number of radial wire locations multiplied by the number of axial wire locations. In the case of the setup shown in Fig. 6, the model included 60 columns and eight rows in the Green's matrix.

B. Experimental calibration

Due to limitations in the magnetostatic simulation of our thruster, calibration is accomplished experimentally. A holder

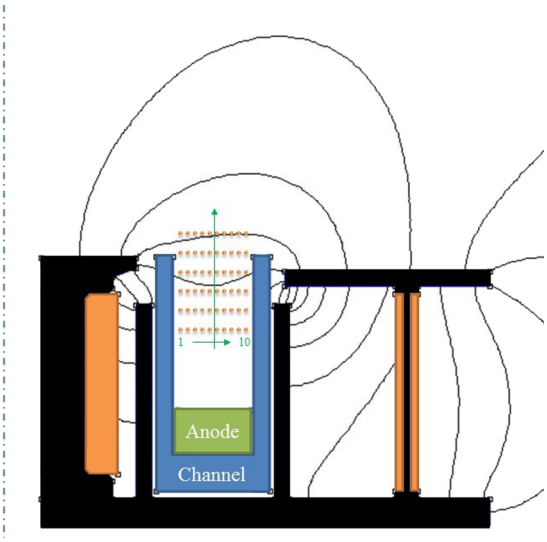

FIG. 6. FEMM calibration simulation. The 10 copper wires are shown in the channel and numbered 1 through 10. The wires are moved further downstream as the calibration progresses.

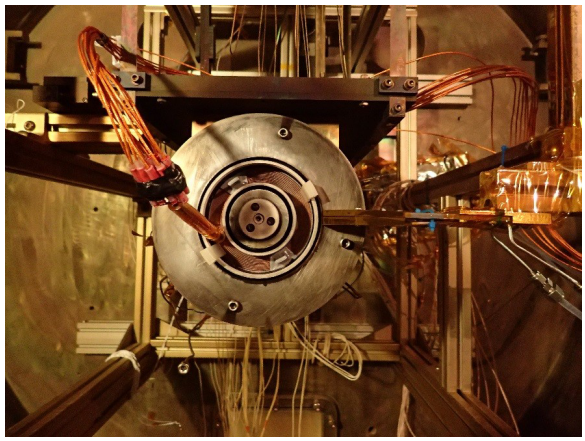

FIG. 7. Calibration coil in CSU HET. The calibration coils are shown placed at one of the axial positions during the calibration process with the sensor array at the 3 o'clock position.

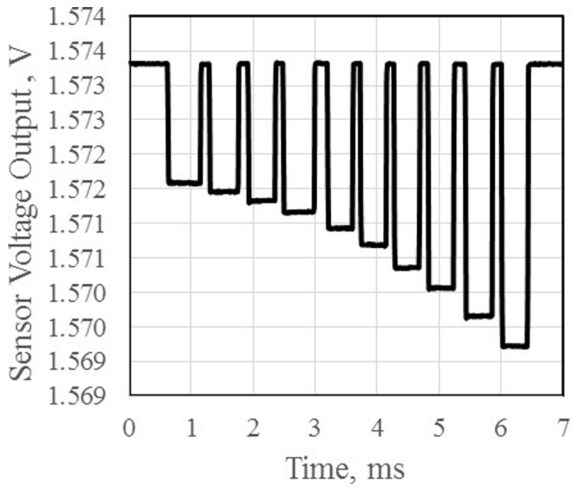

FIG. 8. Sample calibration output. An example of the voltage output of a sensor as each radial coil is individually energized.

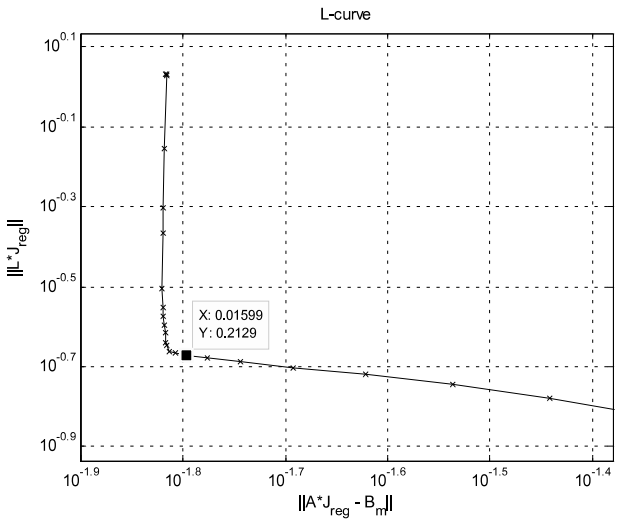

FIG. 9. L-curve Plot. Testing method used to choose the optimal regularization parameter for the inverse solution.

with ten 22 gauge copper magnet wires was designed to fit inside the ceramic channel of the HET, shown in Fig. 7. The thruster inner coil and outer coils are energized and powered through the entire calibration process while a current was applied sequentially to each calibration wire. A background measurement was first acquired for each axial position of the calibration coils. The axial location of the coil was set using a spacer that rested between the anode and the calibration coil. A LabVIEW program recorded the output voltage of the sensor as each wire had current applied. For the 10-wire calibration coil, a measurement for one single sensor at one axial location would look similar to Fig. 8. Each step in Fig. 8 represents applying current to one of the radial wires. The first radial wire was located near the inner channel wall, furthest from the sensor. The largest step corresponded to the wire nearest the outer channel wall, and therefore, closest to the sensor. The increase in the sensor output as the source of the induced current nears the sensor was as expected. The voltage decreased each time a coil was charged. The resistance of the sensor increased due to the induced field and the voltage drop across the passive resistor decreases, respectively.

The stationary 8-sensor array allowed for a simplified calibration process compared to a moveable sensor array. Since all 8 sensors are already at the desired measurement locations and they are sampled simultaneously, the radial coils only need to be moved for each axial location. The calibration data were then used to create the Green's matrix in the same way as described in the simulated calibration.

C. Inverse solution

The calibration process has the sole purpose of generating the A matrix shown in Eq. (3) for the inverse problem. A Matlab script was written using the "fmincon" function to execute the constrained minimization algorithm and solve Eq. (3). The current density solution obtained was a row vector of length equivalent to the number of radial calibration coils multiplied by the number of axial calibration locations. This vector was then reshaped to obtain a contour plot of the current distribution. The regularization term, λ, determines the amount of second-order smoothing applied to the current density distribution. The inverse solution process is set to solve the problem over an even-space logarithmic range of regularization parameters. The discrete smoothing norm and residual norm are plotted against each other, and they display an L-curve shape as shown in Fig. 9. The minimum point of the two parameters forms a bend at which the optimal amount of regularization can be found. A small regularization value can lead to a solution that is discontinuous and not representative of a realistic distribution. Too large of a regularization parameter can lead to an abundance of smoothing and yield a generic bell-curve distribution, sacrificing resolution of fine features in the solution. The regularization term was determined from the sample averaged data obtained in the calibration process. The same regularization term was then used to determine current density from the raw data, down-sampled to 500 kHz. This process takes significant computational time (~10 h for 50,000 data points) but provides temporally varying 2D images of the Hall current structure within the thruster channel. A limited study analyzed the validity of using a single regularization parameter over a small period of a data set. In this study, the optimal regularization parameter was calculated for each time step.

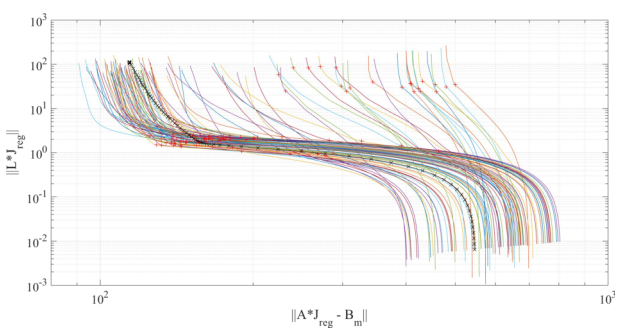

FIG. 10. Averaged and individual L-Curves. 400 μs of data down-sampled to 250 kHz that were measured with the HET operated at 1.6 kW.

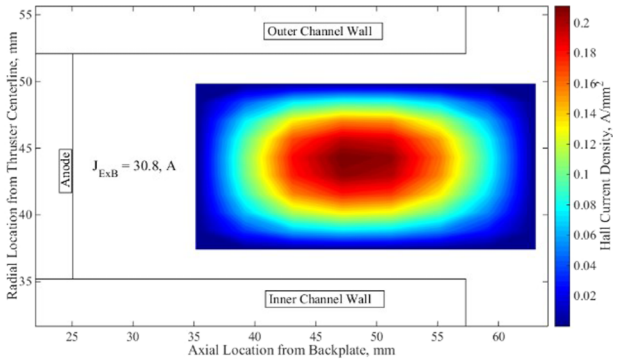

FIG. 11. Hall current density distribution. 100 ms time-averaged contour plot of the Hall current density at 1.3 kW operation at 4.85 A discharge current.

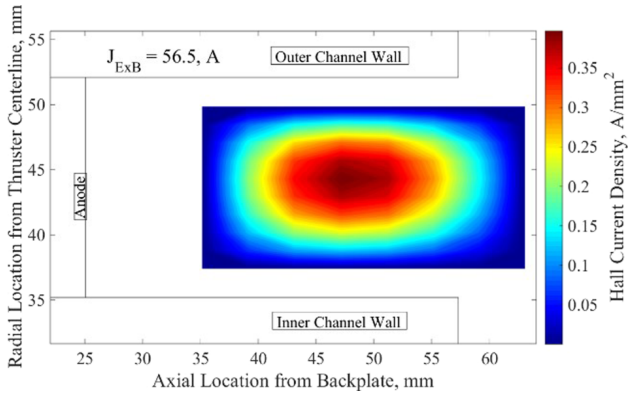

FIG. 13. Hall current density distribution. 100 ms time-averaged contour plot at 2.2 kW operation and 7.41 A discharge current.

The results, shown in Fig. 10, demonstrated that the average regularization parameter agreed well with a majority of the time steps; however, the time steps where the Hall current reached a minimum value corresponded to erroneous L-curves that did not agree with the other time steps. This is most likely due to the decreased signal-to-noise ratio at times when the Hall current density is low. While this trend warrants further study, the use of an averaged L-curve was deemed acceptable for this work due to the agreement with the majority of the time steps and the computational limitations of the project.

IV. RESULTS AND DISCUSSION

A. Time-averaged, 8-sensor array results

Several measurements were made with the CSU HET at different operating conditions. All of the data acquired during calibration and testing were sampled at 2 MHz for 0.1 s (200,000 samples per channel). The results were time-averaged before generating the Green's matrix and processing the inverse solution. As mentioned above, this was done because calculating the optimal regularization parameter for every sample in the temporal solution would take a significant amount of computational resources. The averaged measurements provide a good regularization parameter to be used in the temporal solution as well as yielding an average azimuthal current.

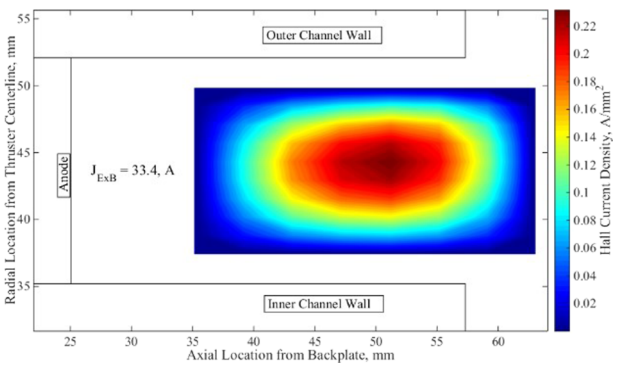

FIG. 12. Hall current density distribution. 100 ms time-averaged contour plot of the Hall current density at 1.6 kW operation at 5.46 A discharge current.

The current distribution was spread out over a large fraction of the calibration domain, as shown in Figs. 11 to 13. The shape of the Hall current is elongated in the axial direction due primarily to these results being time averaged. This axial spread is indicative of the motion of the Hall current during sampling. The Hall current also exhibits a linear relationship with respect to the discharge current, as expected (Fig. 14).

B. Temporal solution

The data collected during the 8-sensor array tests were acquired at a rate of 2 MHz and every 4 points are averaged to achieve some smoothing, which results in a sampling frequency of 500 kHz. The motion of the Hall current density within the channel can be seen in the series of images in Fig. 15. The time between total current minimums was 42 μs, suggesting a fundamental frequency of ~24 kHz. The breathing mode of the thruster based on discharge current oscillation measurements during stable operation was at a frequency between 26 kHz and 28 kHz, in good agreement with the imaging results. We expect that the Hall current will follow the breathing mode oscillations because the plasma density has a first order dependency with respect to the neutral density. The minimum current density distribution shown in the last image still indicated

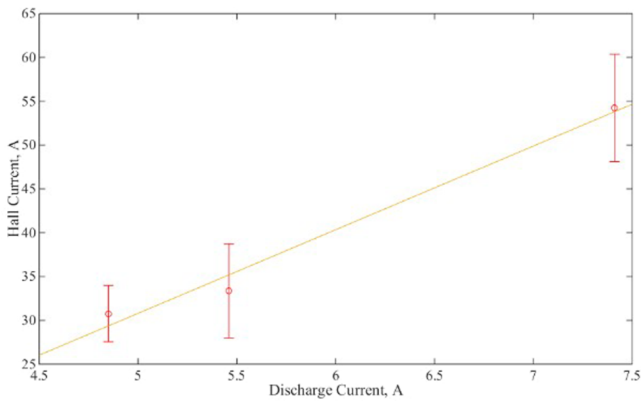

FIG. 14. Hall current vs. discharge current. The average currents shown in Figs. 11–13 are plotted against the corresponding average discharge current with a linear fit. Error bars represent 95% confidence interval.

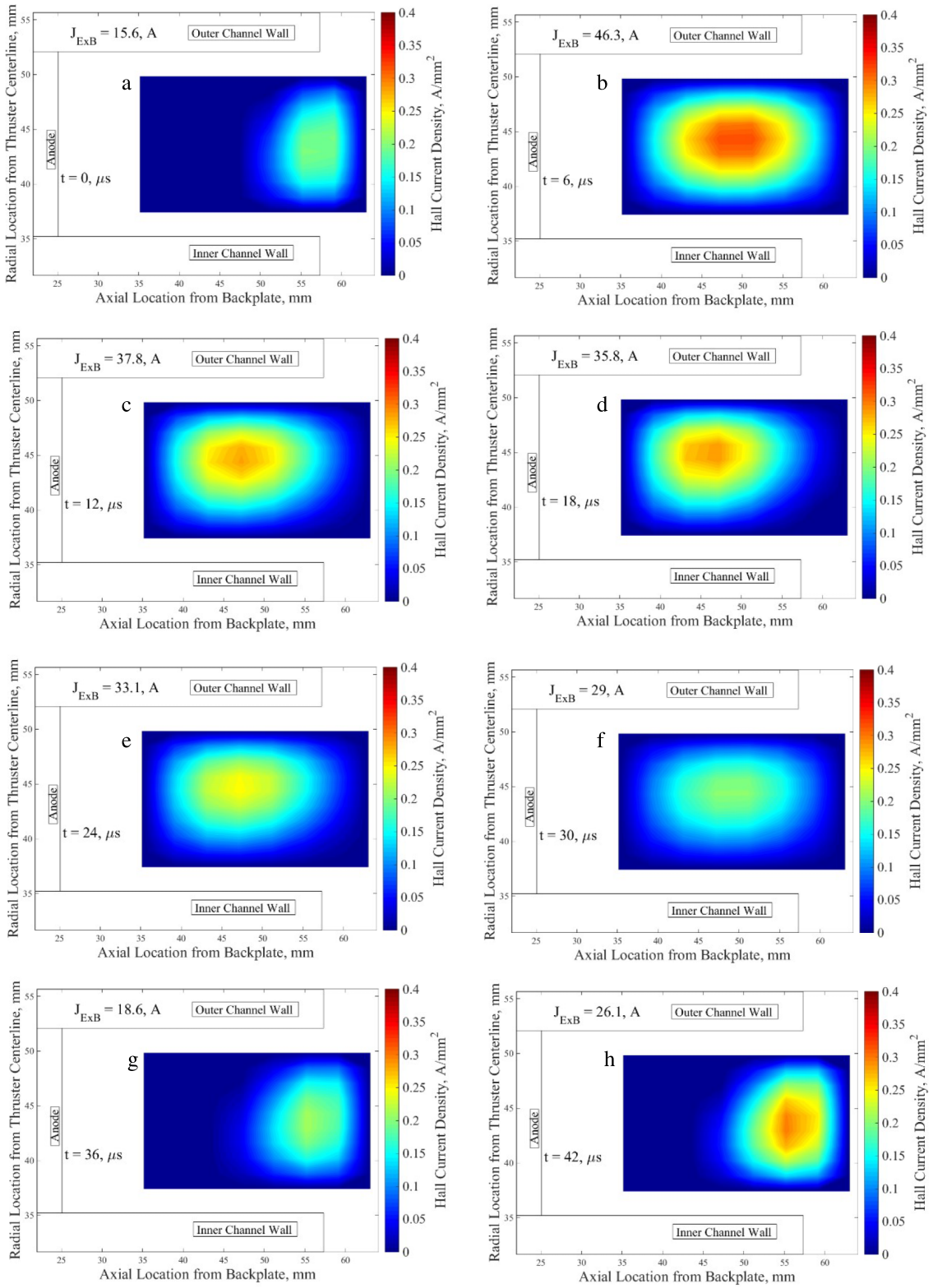

FIG. 15. Sequential images of CSU HET Hall current oscillation. Nominal operating conditions, Vd = 300 V, $I_d = 5.46$ A, $\dot{m} = 4.0$ mg/s of krypton. Time between images is 6 μs.

a measureable current as expected. As ions are expelled from the channel during the neutral refill time, a residual current will still remain from the electrons supplied by the cathode as the thruster waits for the neutrals to refill the channel to start the cycle process all over again. As the neutrals replenish and the Hall current grows, the ionization region (images 15a to 15c) moves upstream. The Hall current varies from 2.9 to 8.5 times the average discharge current over the breathing cycle. The strong agreement between the measured breathing mode and the contour plots following the predator-prey model provides a base level validation of the sensor system.

V. CONCLUSION

We have demonstrated the capability to image the Hall current density and calculate the Hall current using remotely located magnetic sensors and inverse magnetostatic algorithms. The centroid of the Hall current density was observed to move axially from a location of 10 mm upstream to 5 mm downstream of the exit plane of the channel at a thruster power of 1.6 kW. In addition to temporal and spatial changes in the Hall current density structure, the Hall current was found to vary with time over a range from 19 A to 48 A with a fundamental frequency of 24 kHz, which is in good agreement with breathing mode frequencies determined from temporal measurements of the discharge current. The combination of these observations suggests that the Hall current imaging system has successfully resolved the breathing mode of the discharge plasma. Future work will focus on determining the effects of gas type, mass flow rate, magnetic field configuration, and discharge current and voltage on Hall current density structure and magnitude. Channel magnetic field maps will also be used in combination with the Hall current density measurements to calculate the thrust and compare with thrust stand values. Use of the system in combination with synced high speed cameras and discharge current measurements is planned to characterize breathing mode and higher frequency instabilities within the Hall thruster channel. The present calibration method is performed manually with the thruster at room temperature, which may result in offset errors due to thermal effects once the thruster reaches steady state operation. To mitigate these errors we plan to develop an automated calibration method that can be performed on a thruster immediately after being operated. In addition, we plan to increase the number of axial calibration locations and improve the inverse solution algorithm boundary conditions to reduce the solution bias and provide measurements over the entire channel domain. Further study of the impact of the number of calibration locations and optimization of the sensor placement on the solution accuracy would further improve the system. One of the main advantages of our Hall current imaging system is that detailed movement of the Hall current structure can be obtained at a frame rate up to 2 MHz. We believe that this information will enable discovery of magnetic field geometry, neutral injection methods, anode configuration, and power supply topology that will improve thruster performance, quench instabilities, and help explain and quantify facility effects.

ACKNOWLEDGMENTS

This research was supported in part by the Air Force Institute of Technology (Grant No. FA8601-14-P-0011).

[1]J. M. Haas and A. D. Gallimore, "Considerations on the role of the Hall current in a laboratory-model thruster," AIAA Paper 2001-3507, 2001.
[2]J. A. Linnell and A. D. Gallimore, "Hall thruster electron motion characterization based on internal probe measurements," in 31st International Electric Propulsion Conference, 2009.
[3]C. A. Thomas, N. Gascon, and M. A. Cappelli, "Nonintrusive characterization of the azimuthal drift current in a coaxial E × B discharge plasma," Phys. Rev. E **74**, 056402 (2006).
[4]A. N. Ermilov, V. F. Eroshenkov, D. N. Novichkov, Y. A. Kovalenko, T. M. Sapronova, T. V. Chernyshev, and A. P. Shumilin, "Oscillations of the Hall current in a Hall thruster with an anode layer," High Temp. **52**, 360–365 (2014).
[5]A. I. Bugrova, V. S. Versotskii, and V. K. Kharchevnikov, "Determination of the radial center of gravity of an azimuthal drift current in accelerators with closed electron drift," Sov. Phys. Tech. Phys. **25**(10), October 1980.
[6]V. N. Dem'yanenko, I. P. Zubkov, S. V. Lebedev, and A. I. Morozov, "Induction method for measuring the azimuthal drift current in a Hall-current accelerator," Sov. Phys. Tech. Phys. **23**(3), March 1978.
[7]R. Binyamin, "Analysis and numerical experimentation of onboard diagnostic systems for Hall thrusters," Ph.D. thesis, Israel Institute of Technology, 2006.
[8]R. A. Martinez, C. R. Mullins, J. Moritz, J. D. Williams, and C. C. Farnell, "Performance evaluation of a 1.5 kW Hall effect thruster with a center mounted heaterless hollow cathode using xenon and krypton propellant," CSU Electric Propulsion and Plasma Engineering Lab, 2015 (unpublished).
[9]M. D. Cubells, C. Reig, A. De Marcellis, A. Roldan, J. B. Roldan, S. Cardoso, and P. P. Freitas, "Magnetic tunnel junction (MTJ) sensors for integrated circuits (IC) electric current measurement," in 2013 IEEE Sensors Proceedings, 2013.
[10]S. Łęski, K. H. Pettersen, B. Tunstall, G. T. Einevoll, J. Gigg, and D. K. Wójcik, "Inverse current source density method in two dimensions: Inferring neural activation from multielectrode recordings," Neuroinformatics **9**, 401–425 (2011).
[11]H. Saotome and Y. Saito, "Locally orthogonal coordinate systems for analyzing inverse problems of magnetostatic fields: Applications to magnetocardiogram and magnetoencephalogram," IEEE Trans. Magn. **29**, 3343–3345 (1993).
[12]M. Yan, S. Udpa, S. Mandayam, Y. Sun, P. Sacks, and W. Lord, "Solution of inverse problems in electromagnetic NDE using finite element methods," IEEE Trans. Magn. **34**, 2924 (1998).
[13]O. Chadebec, J. L. Coulomb, J. P. Bongiraud, G. Cauffet, and P. Le Thiec, "Recent improvements for solving inverse magnetostatic problem applied to thin shells," IEEE Trans. Magn. **38**, 1005–1008 (2002).
[14]J. Weese, "A reliable and fast method for the solution of Fredhol integral equations of the first kind based on Tikhonov regularization," Comput. Phys. Commun. **69**, 99–111 (1992).
[15]P. C. Hansen and D. P. O'Leary, "The use of the L-curve in the regularization of discrete III-posed problems," SIAM J. Sci. Comput. **14**, 1487–1503 (1993).
[16]C. A. Thomas, N. Gascon, and M. A. Cappelli, "A study of the azimuthal electron drift in an E × B discharge using a non-invasive antenna array," AIAA Paper 2003-4854, 2003.